# Structure-properties phase diagram for La$_{1-x}$Sr$_x$MnO$_3$ (0.1≤x≤0.2)

B. Dabrowski, X. Xiong, Z. Bukowski, R. Dybzinski, P. W. Klamut, J. E. Siewenie, O. Chmaissem, J. Shaffer,
and C. W. Kimball

*Department of Physics, Northern Illinois University, DeKalb, Illinois 60115*

J. D. Jorgensen and S. Short

*Materials Science Division, Argonne National Laboratory, Argonne, Illinois 60439*

(Received 10 March 1999)

By combining the results of magnetization, resistivity, and neutron powder-diffraction data for stoichiometric La$_{1-x}$Sr$_x$MnO$_3$, we have constructed a phase diagram that describes the magnetic, transport, and structural properties and the relationships among them as a function of composition (0.1≤x≤0.2) and temperature (10–340 K). We show that, with increasing Sr content, the Curie temperature increases linearly, while the temperature of an orbital ordering transition to a state with a large coherent Jahn-Teller (JT) distortion decreases. These two phase-transition lines cross at $x=0.145$ and $T=210$ K. When the transition to the ferromagnetic state occurs in a phase that has a large coherent JT distortion ($x<0.145$), a strong magnetolattice coupling is observed; the coherent JT distortion is dramatically reduced and the incoherent distortion is enhanced in the ferromagnetic phase. For $x>0.145$, where the coherent JT distortion is small above Curie temperature, magnetolattice coupling reduces the incoherent distortion at $T_C$ and strongly suppresses the transition to a phase with a large coherent JT distortion. These observations are consistent with a competition between ferromagnetism and JT distortion that is mediated by a colossal spin-charge-lattice coupling. A metallic state occurs below the Curie temperature when both coherent and incoherent JT distortions are suppressed. [S0163-1829(99)14933-6]

## INTRODUCTION

Pure and substituted La$_{1-x}$Sr$_x$MnO$_3$ materials are of considerable current interest owing to a very large spin-charge-lattice coupling that causes a colossal magnetoresistive effect for the ferromagnetic phase ($x\geq0.1$) near the Curie temperature, $T_C$.[1] For LaMnO$_3$, molecular orbital theory in accordance with the Pauli exclusion principle predicts a high-spin electronic configuration $t_{2g}^3 e_g^1$ for the Mn$^{3+}$ ions ($d^4$) with corelike $t_{2g}$ states and extended $e_g$ orbitals.[2–5] This electronic configuration is susceptible to a strong electron-phonon coupling of the Jahn-Teller (JT) type that splits the $e_g$ states into filled $d_{z^2}$ and empty $d_{x^2-y^2}$ orbitals, and, thus, produces large asymmetric oxygen displacements. In addition, the magnetic superexchange interaction produces ferromagnetic coupling within the Mn-O planes between JT-ordered orbitals of dissimilar symmetry and antiferromagnetic coupling perpendicular to the planes between orbitals of the same symmetry. The resulting in-plane orbital ordered and the $A$-type three-dimensional antiferromagnetic structures were observed in both the long-range[6–9] and short-range[10] measurements.

With Sr substitution, a fraction of electrons is removed from the $d_{z^2}$ orbital causing weakening of both the JT-electron-phonon coupling and the superexchange interaction. Empty states in the $e_g$ orbitals also allow for spin-dependent electron hopping leading to a double-exchange ferromagnetic interaction and metallic conductivity.[4,5,11] In addition, however, electron-phonon coupling of the charge-ordered type is possible and can produce large symmetric oxygen-atom displacements and charge localization. Competition between these various magnetic and electron-phonon interac-

tions results in a very rich structure-property phase diagram for moderately substituted La$_{1-x}$Sr$_x$MnO$_3$ materials, $0.1\leq x \leq0.2$.[12–15] Recent theoretical work indeed shows that the explanation of the transport and magnetic properties requires consideration of all magnetic and electron-phonon interactions.[16–18]

Upon substitution of Sr, La$_{1-x}$Sr$_x$MnO$_3$ transforms from an antiferromagnetic insulator to a ferromagnetic insulator at $x\approx0.1$ and to a ferromagnetic metal at $x\approx0.16$.[12–15] The Curie temperature increases with Sr substitution from $\sim$150 K for $x\approx0.1$ to $\sim$300 K for $x\approx0.2$. Reported values of the compositions and temperatures for the magnetic and resistive transitions vary substantially in the literature, depending on the sample processing method and synthesis conditions.[19]

Three distorted structural phases of the cubic perovskite structure have been identified at room temperature as a function of Sr substitution level for $0\leq x\leq0.2$.[6–9,12,13,19] For pure and lightly substituted materials, the orthorhombic *Pbnm* structure ($O'$), characterized by large coherent orbital ordering of the JT type and $c/a<\sqrt{2}$, was found.[6–9,12,13] The coherent JT distortion decreases with increased Sr substitution level.[12,13] Above $x\approx0.08-0.12$, a phase ($O^*$) with the same orthorhombic *Pbnm* structure but characterized by a considerably smaller coherent JT-orbital ordering and $a\approx b\approx c/\sqrt{2}$ is observed.[12,13] Structural analysis by the pair-distribution function technique indicates that large incoherent JT distortions are still present for this phase.[20] At higher Sr substitution level, $x\approx0.16-0.18$, the rhombohedral $R\bar{3}m$ structure ($R$), characterized by the absence of a coherent JT orbital ordering, was observed; i.e., all Mn-O bonds have equal length for this phase.[21,22] A structural phase transfor-

mation induced by an external magnetic field was found for $x = 0.17$, supporting a picture of strong coupling of the local spin moments and the charge carriers to the crystal lattice.[23]

Complex relationships among the structural, magnetic, and charge-ordering transitions have been observed below room temperature. Neutron-diffraction studies have shown that the ferromagnetic ordering suppresses the coherent JT distortion of the $O'$ phase, suggesting a strong coupling between asymmetric distortion of the Mn-O bond lengths, the ferromagnetic ordering, and the transport properties.[13] A reentrant structural transformation on cooling, from $O^*$ to $O'$ and back to $O^*$, has been reported for $x \approx 0.125$.[13,24] For similar compositions, a transition to a charge-ordered phase, characterized by a commensurate structure with $2a \times 2a \times 4a$ (where $a$ is the cubic perovskite lattice parameter) was observed for large single crystals.[25] Rapid increases of resistivity corresponding to charge ordering were seen for single crystals and bulk samples.[14,24] Again, the reported values of the compositions and temperatures for the various transitions vary in the literature among different researchers.[12–15,19,24] Moreover, various phase diagrams were constructed using physical and structural information obtained for dissimilar samples.

The discrepancies among existing phase diagrams may result from comparing the behavior of compositions that are incorrectly assumed to have the same doping level.[26,27] The resistivity, $T_C$, and structural properties can depend, in addition to the Sr substitution level, on chemical stoichiometry that is a function of the synthesis conditions.[26–31] Research on pure and substituted LaMnO$_3$ has shown that there can be large deviations from nominal stoichiometry that are caused by the formation of vacancies on the metal sites while the oxygen network is believed to remain undefected.[28–31] For low and moderate substitution levels ($0 \leq x \leq 0.3$), the perovskite structure can form a large concentration of vacancies, $v$, on both the $A$ (La, Sr, etc.) and $B$(Mn) sites during synthesis under oxidizing conditions. Formation of vacancy defects on the $A$ and $B$ sites in equal numbers would increase the average Mn oxidation level by $\sim 6v$. Because a variety of synthesis conditions have been employed, for example, annealing at high oxygen pressure at $650\,°C$,[32] or annealing in air at $1400\,°C$ followed by quenching or furnace cooling,[33] it is not surprising that the hole doping (the average Mn oxidation level), $h \approx x + 6v$, may differ considerably for samples made with the same $x$. Additionally, vacant metal sites on the electronically active Mn-O network can produce charge localization and cause local displacements of the oxygen ions that may be improperly interpreted as resulting from electron-phonon interactions. Since the physical and structural properties are complex and are very sensitive to the hole concentration,[12–16,19] it is of critical importance to establish the intrinsic phase diagram as a function of the hole doping; i.e., a function of the Sr substitution level for samples that contain no metal-site vacancies ($v \approx 0$).

We report here a study of the resistive, magnetic, and structural properties of homogenous La$_{1-x}$Sr$_x$MnO$_3$ ($0.1 \leq x \leq 0.2$) samples prepared in air under thermodynamic conditions, determined by thermogravimetric measurements, that assure the synthesis of stoichiometric material. The phase diagram shown in Fig. 1 summarizes the magnetic, transport, and structural properties as a function of composition and
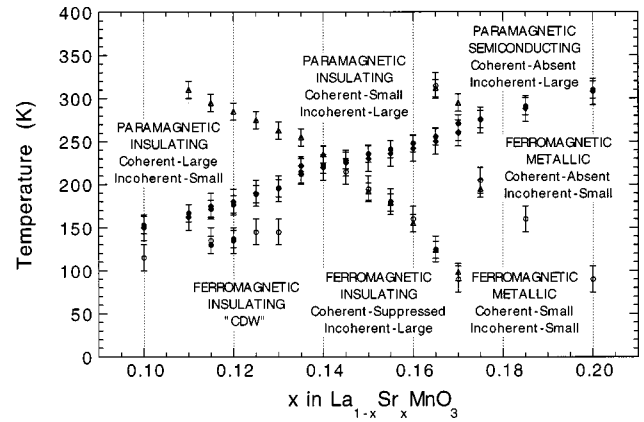


FIG. 1. Phase diagram summarizing the magnetic, transport, and structural properties of La$_{1-x}$Sr$_x$MnO$_3$ as a function of composition, $0.1 \leq x \leq 0.2$, and temperature, $10 \leq T \leq 350$ K. The marks denote: temperatures of anomalies in resistance caused by the ferromagnetic (filled diamond) and structural-electronic (open triangle) transitions, temperatures of ferromagnetic transitions obtained from magnetization measurements (filled circles), temperatures of decreased-magnetization anomalies caused by the structural-electronic transitions (open circles).

temperature. With increasing Sr content, the Curie temperature increases, while the structural transition temperatures from $O^*$ to $O'$ (large coherent JT-orbital ordering) and $R$ to $O^*$ (small coherent JT-orbital ordering) decrease. Crossing of magnetic and structural phase-transition lines results in six distinct phases with various interrelated structural and physical properties as shown in Fig. 1. In addition, a highly resistive phase, compatible with a charge-ordered state, with a reduced magnetic moment but no clear signature of superstructure ordering in powder diffraction can be identified below 150 K near $x \sim 0.125$. For $x < 0.145$ a strong magnetolattice coupling below the Curie temperature suppresses the coherent JT distortion of the orthorhombic $O'$ phase but in turn increases the incoherent JT distortion. For $x > 0.145$ the ferromagnetic transition is accompanied by a slight decrease of the incoherent JT distortion for the orthorhombic $O^*$ and rhombohedral $R$ phases. These results confirm that an insulating phase is formed above $T_C$ as a result of polaronic, coherent or incoherent, JT-induced charge localization in addition to the spin scattering.[16,17] The structural transformation from the $O^*$ to the $O'$ phase is strongly suppressed in the ferromagnetic region for $x > 0.145$. The observed features point to a competition between ferromagnetism and JT distortion that is mediated by a colossal spin-charge-lattice coupling.

## SAMPLE PREPARATION AND EXPERIMENTAL DETAILS

Polycrystalline samples of La$_{1-x}$Sr$_x$MnO$_3$ with $0.1 \leq x \leq 0.2$ and $\Delta x = 0.005$, were synthesized from $\sim 10$ g batches of a stoichiometric mixture of La$_2$O$_3$ (dried in Ar at $700\,°C$), MnO$_2$ and SrCO$_3$ that were initially ground and fired at $800\,°C$ in air. Samples were dissolved in citric and nitric acids on a hot plate. Ammonium hydroxide was added to obtain a complex citrate solution, pH$\approx 5$. The solution was dried at $200-300\,°C$ and decomposed in air at $500-800\,°C$.
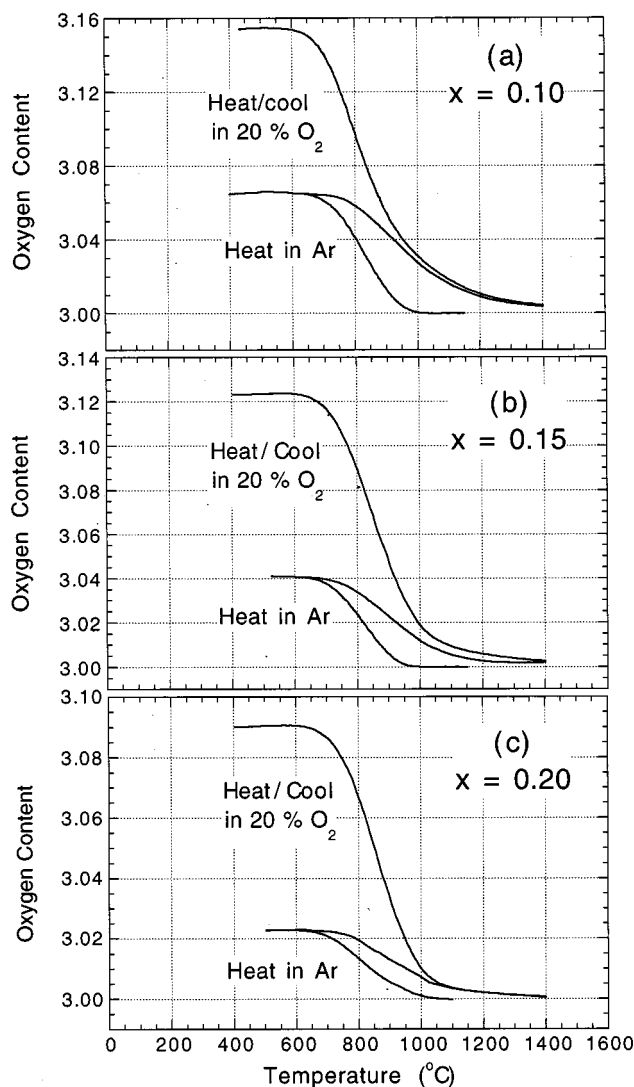
FIG. 2. Oxygen contents in 20% $O_2$ and Ar from thermogravimetric measurements for $La_{1-x}Sr_xMnO_3$ samples with $x = 0.10$ (a), 0.15 (b), and 0.20 (c) annealed at 120 atm. $O_2$ at 800 °C.

Sintering was done in air at 1400 °C for a day. Samples were ground, pressed into pellets, and fired in air at 1450–1350 °C overnight followed by a fast cooling to room temperature on a Cu plate. This wet-chemistry method leads to dense samples with homogenous mixing of the metal ions.

The final firing temperatures and oxygen atmosphere as well as holding times and cooling rates for obtaining stoichiometric samples were determined from thermogravimetric analysis (TGA) measurements performed using a high sensitivity Cahn TG 171 system with slow heating (2 deg/min) and cooling (0.6 deg/min) rates. After synthesis in air at 1400 °C, parts of the samples were annealed at 120 atm $O_2$ at 800 °C for two days and fast cooled to room temperature. About 1 g powdered samples were subjected to two consecutive TGA runs: First, samples were slowly heated to 1400 °C and then cooled to room temperature in a 20% $O_2$/Ar gas mixture; and second, samples were slowly heated to 1150 °C and fast cooled to room temperature in pure Ar ($\sim 10$ ppm $O_2$). Figure 2 shows the oxygen contents from TGA data for $La_{1-x}Sr_xMnO_3$ samples with $x = 0.10$, 0.15, and 0.20. The oxygen content was assumed to be 3.000

$\pm 0.002$ per molecule of $La_{1-x}Sr_xMn$ at the center of extended weight plateau observed in TGA data at 1100 °C in Ar. This assignment was based on the weight losses measured by TGA in 50% $H_2$/Ar for $LaMnO_3$ and $La_{1-x}Ca_xMnO_3$ materials where the reduction products are stoichiometric $La_2O_3$ and $Ca_{x/(1+x)}Mn_{1/(1+x)}O$ compounds and, thus, oxygen content can be calculated very accurately. For the $La_{1-x}Sr_xMnO_3$ system, the reduction products contain a nonstoichiometric $La_{2-y}Sr_yMnO_{4-\delta}$ phase ($y$ and $\delta$ are not known exactly); i.e., a confirmation of the absolute oxygen content as being 3.000 in Ar at 1100 °C cannot be done as precisely as it was done for the $La_{1-x}Ca_xMnO_3$ materials.[34]

Figure 2 shows that the starting materials annealed at high oxygen pressure as well as materials obtained after slow cooling in 20% $O_2$ have effective oxygen contents substantially above 3. Since, in actuality, there is no excess oxygen above 3 in the structure, but vacancies form on both metal sites $A$ and $B$, the vacancy concentration can be estimated (assuming equal amounts on both sites) as $v \approx d/(d+3)$. The observation of large effective oxygen contents clearly demonstrates that significant increases of the doping level are created for materials annealed in oxygen-rich atmospheres at 700–1200 °C. In addition, these large vacancy concentrations may introduce local structural displacements and electronic inhomogeneity that would affect structural, magnetic, and transport properties, complicating understanding of the intrinsic properties of the materials.

The TGA data on heating and cooling in 20% $O_2$ was quite reproducible in the temperature range 1100–1400 °C; i.e., samples were near thermal equilibrium when slowly heated and cooled. Weights of the samples approached stable levels indicating oxygen contents of $3.002 \pm 0.002$ for temperatures above 1400, around 1400, and 1350 °C for $x = 0.10$, 0.15, and 0.20, respectively. The changes of the oxygen contents close to these temperatures (within $\pm 50$ °C) were very small, less than 0.002. Since our aim was to prepare stoichiometric samples within the range of compositions $0.1 \leq x \leq 0.2$ we could use firing in Ar at 1100 °C followed by fast cooling or firing in air followed by quenching from 1450 °C for $x = 0.10$, and gradually lower temperatures for samples with larger $x$, to 1350 °C for $x = 0.20$. The $La_{1-x}Sr_xMnO_3$ samples prepared in Ar at 1100 °C have shown very large resistivity probably due to a presence of the decomposed material at the grain boundaries. For that reason we have chosen to synthesize stoichiometric $La_{1-x}Sr_xMnO_3$ samples in air. The nearly stoichiometric compositions, $d \leq 0.003$, were confirmed for these air-quenched samples by performing additional TGA measurements in 20% $O_2$ and Ar.

The purity of samples was checked by powder x-ray diffraction at room temperature after every firing and thermogravimetric (TGA) measurement, confirming single-phase material in each case. All samples prepared in air at 1450–1350 °C showed clean x-ray-diffraction patterns with sharp peaks corresponding to the expected orthorhombic and rhombohedral structures. At room temperature the $x = 0.10$ sample is orthorhombic-$O'$ and a transition from the orthorhombic $O'$ to the $O^*$ structure occurs around $x = 0.11$. The $x = 0.11$ sample is mixed phase, mostly with the $O'$ struc-

ture. The $x=0.115$ composition is also mixed phase, mostly $O^*$. Compositions from $x=0.12$ to 0.165 are pure orthorhombic $O^*$. A transition from the orthorhombic $O^*$ phase to rhombohedral phase occurs for the $x=0.17$ composition. The sample is mixed phase $O^*$ and $R$ in about equal amounts. Above $x=0.17$, samples are rhombohedral.

Neutron powder-diffraction data were obtained using the Special Environment Powder Diffractometer (SEPD) at Argonne National Laboratory's Intense Pulsed Neutron Source.[35] The powder samples were contained along with helium exchange gas in indium-sealed vanadium cans and cooled on a Displex closed-cycle refrigerator. Data were taken at closely spaced temperatures from 15–345 K with sufficient statistics at each temperature to provide accurate refinements of atom positions and temperature factors. This required 2–4 h data collection times at each temperature. Magnetization and resistivity measurements were performed with a Quantum Design physical properties measurement system.

## MAGNETIC AND RESISTIVE PROPERTIES

The structure-properties phase diagram shown in Fig. 1 was constructed by combining the results of dc magnetization, ac susceptibility, resistivity, and structural measurements. The phase transitions were found to exhibit distinctive signatures in each kind of measurement. In the following sections, the individual measurements are described in detail to illustrate how the phase transitions are identified. The combination of measurements allows the correlated transport, magnetic, and structural phenomena to be characterized for each kind of phase transition that occurs in this system.

Magnetic properties of all samples were studied using dc magnetization and ac susceptibility measurements in small (~20 Oe) and large (3 T) applied magnetic fields. A full description of the magnetic measurements together with the data on the magnetic structures that were determined by the neutron powder diffraction will be published elsewhere.[36] Here, we focus attention on two main magnetic properties: The clearly visible ferromagnetic transition and the less apparent decreased-magnetization anomaly frequently observed below $T_C$.[37] Both transitions can be precisely defined for small magnetic fields. These magnetic transitions have been correlated with the resistive and structural transitions to construct the structure-properties phase diagram (Fig. 1).

Magnetization data obtained on cooling in a 20 Oe applied field are shown in Fig. 3 for $La_{1-x}Sr_xMnO_3$ samples with compositions near the previously reported charge ordering transition, $x \approx 0.125$.[25] Samples show reasonably sharp ferromagnetic transitions with $T_C$'s, defined as the temperatures for which the $M(T)$ curves have the largest slope, at 170, 177, and 196 K for $x=0.11$, 0.12, and 0.13, respectively. All other samples for which a ferromagnetic transition appears in the orthorhombic $O'$ structure ($x<0.145$) show similarly sharp transitions with $T_C$'s increasing almost linearly with increasing composition. The magnetization curves show, in addition to the ferromagnetic transitions, weak magnetization anomalies at 135 and 145 K for $x=0.12$ and 0.13, respectively, and a very weak anomaly at 120 K for $x=0.11$ sample with transition temperatures defined again from the largest slope of the $M(T)$ curves. These weak
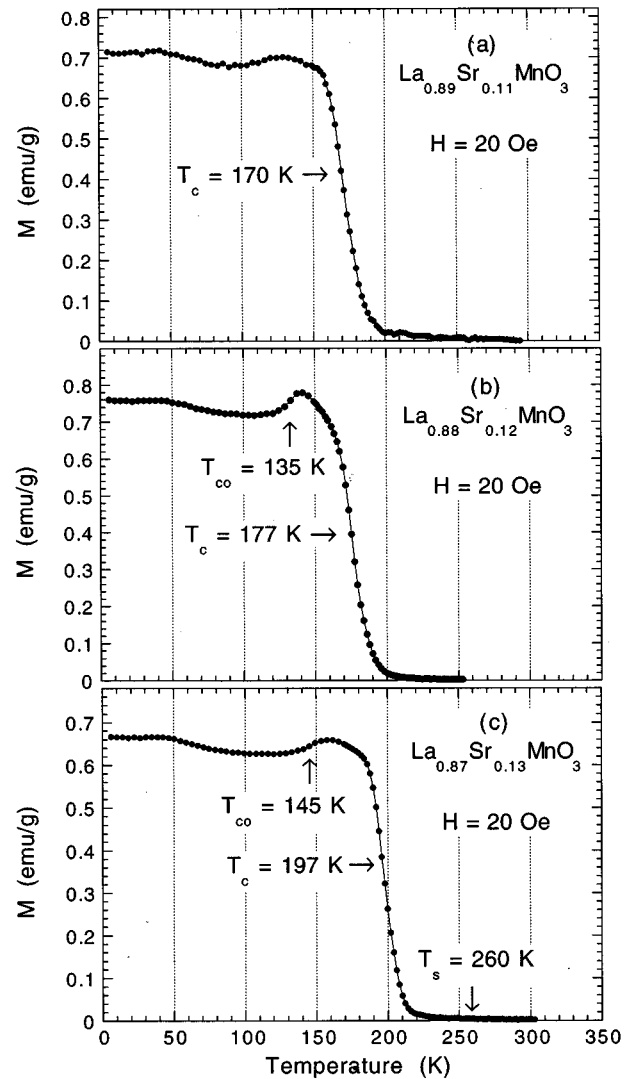


FIG. 3. Magnetization in a 20 Oe applied field for $La_{1-x}Sr_xMnO_3$ samples with compositions near the charge-ordering transition ($T_{c0}$) for which the ferromagnetic transition ($T_C$) appears in the orthorhombic $O'$ structure, $x=0.11$ (a), 0.12 (b), and 0.13 (c).

anomalies mark a decrease of the effective magnetic moment of the bulk samples on cooling.

Figure 4 shows magnetization data for $x=0.155$, 0.16, and 0.165 samples for which the ferromagnetic transition appears in the orthorhombic $O^*$ structure. Ferromagnetic transitions are sharp at 240, 248, and 256 K for $x=0.155$, 0.16, and 0.165, respectively, and continue to increase almost linearly with increasing composition. Again, low-field magnetization curves reveal in addition to ferromagnetic transitions weak magnetization anomalies at 180, 160, and 125 K for $x=0.155$, 0.16, and 0.165, respectively. These anomalies below the Curie temperature correspond to vestiges of the structural $O^*$ to $O'$ transition. Similar decreases of the effective magnetic moment on cooling were observed at systematically decreasing temperatures with increasing $x$ and always correlated very well with resistive transitions and structural transformations.

Figure 5 shows magnetization data for $x=0.175$, 0.185, and 0.20 samples for which the ferromagnetic transition ap-
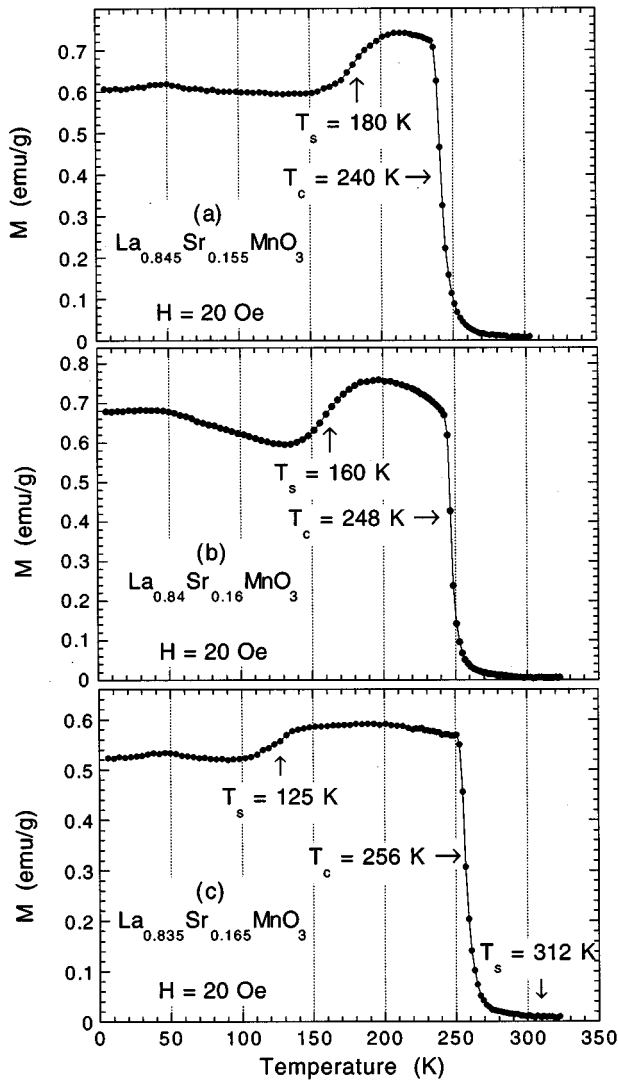
FIG. 4. Magnetization in a 20 Oe applied field for La$_{1-x}$Sr$_x$MnO$_3$ samples with compositions for which the ferromagnetic transition ($T_C$) appears in the orthorhombic $O^*$ structure and the structural $O^*/O'$ transition ($T_s$) appears in the ferromagnetic phase, $x=0.155$ (a), 0.16 (b), and 0.165 (c).

FIG. 5. Magnetization in a 20 Oe applied field for La$_{1-x}$Sr$_x$MnO$_3$ samples with compositions for which the ferromagnetic transition ($T_C$) appears in the rhombohedral $R$ structure and the structural $R/O^*$ transition ($T_s$) appears in the ferromagnetic phase, $x=0.175$ (a), 0.185 (b), and 0.20 (c).

pears in the rhombohedral $R$ structure. These samples show very sharp ferromagnetic transitions at 277, 291, and 310 K, respectively. The low-field magnetization anomalies below the Curie temperature at 200, 160, and 90 K for $x=0.175$, 0.185, and 0.20, respectively, correspond to vestiges of the structural $R$ to $O^*$ transition that shifts to lower temperatures with increasing $x$.

Resistivity was measured using a standard four-lead dc method in zero applied field on cut bars with approximate dimensions $10\times2\times1$ mm. Several temperature-dependent transitions can be seen in Fig. 6 for a series of La$_{1-x}$Sr$_x$MnO$_3$ samples. Starting with the $x=0.10$ composition, two transitions can be observed superimposed on an overall insulating behavior. The upper transition (denoted by a triangle at $\sim325$ K) appears as an increase of resistivity on cooling corresponding to the structural transformation from the $O^*$ to the $O'$ phase.[14,24] This resistive transition, associated with the structural transformation, shifts to lower temperatures with increasing Sr substitution. The second transi-

tion at lower temperatures (denoted by a diamond at $\sim150$ K), during which an exponential increase of the resistivity is distinctly reduced, coincides with the ferromagnetic phase transition. This magnetoresistive transition temperature increases with increasing $x$ and simultaneously becomes better defined as a local drop of resistivity. Values for the structural and magnetoresistive transition temperatures were taken as the temperature of the largest change of resistivity. The ferromagnetic transition temperatures defined in this way are close to the local maximums of resistivity and coincide with the ferromagnetic transition temperatures obtained from magnetization measurements. The structural and ferromagnetic transition temperatures cross around 220 K for compositions between $x=0.14$ and 0.145.

Within the range of compositions of 0.10–0.14, the resistivity displays insulating behavior in both the paramagnetic and ferromagnetic regions. Additional small increases of resistivity on cooling (denoted as dots in Fig. 6) can be conceivably seen at 130 and 135 K for $x=0.115$ and 0.12
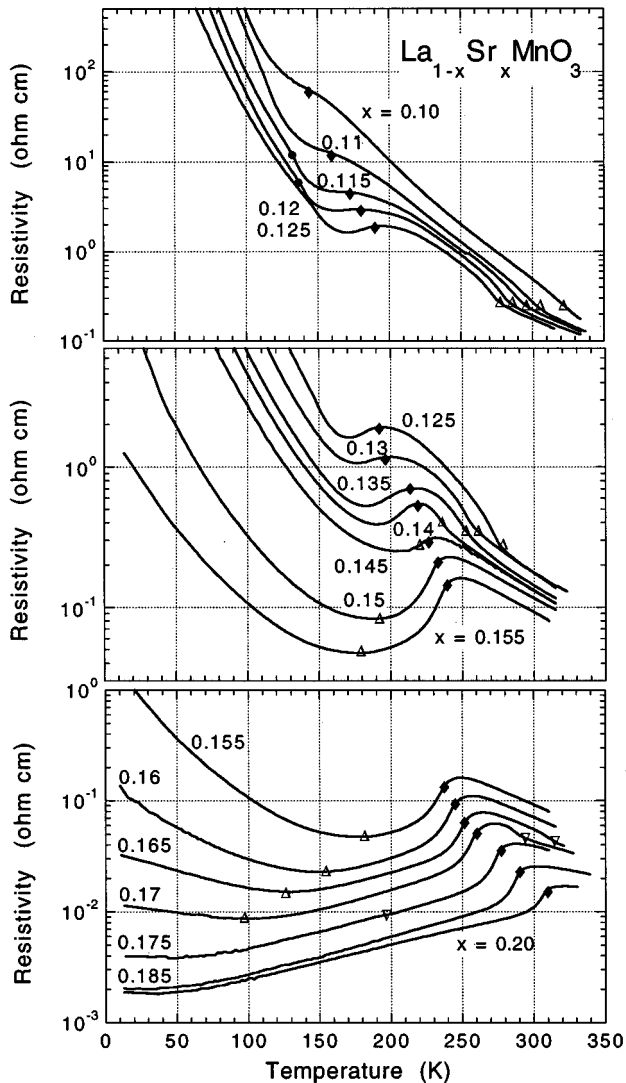
FIG. 6. Resistivities for a series of $La_{1-x}Sr_xMnO_3$ samples, (a) $x=0.10-0.125$, (b) $x=0.125-0.155$, (c) $x=0.155-0.20$. Several transitions are denoted on the resistivity curves: The structural transformation from the $O^*$ to the $O'$ phase (triangle), the structural transition from the $R$ to the $O^*$ phase (inverted triangle), the ferromagnetic transition (diamond), and the charge-ordering transition (dot).

samples, respectively. These increases of resistivity are present at temperatures where a weak decreased-magnetization anomaly was seen for the $x=0.11-0.13$ samples, 130–145 K, and are also in agreement with the resistivity data obtained for single crystals where the effect was clearly visible.[14,24] Most probably, the grain-boundary resistance broadens this (and other) resistive transitions for polycrystalline samples. Since we have not observed any structural anomaly at these compositions and temperatures for our powder samples, we assume that the resistivity and magnetic anomalies are probably caused by the development of a charge-ordered phase near $x=0.125$, for which structural evidence has been reported for large single crystals.[25]

For compositions $x=0.145-0.175$, a gradual development of the metallic phase can be observed below the ferromagnetic transition. The lower temperature boundary of the metallic phase (denoted by a triangle) shifts to successively

decreasing temperatures that can be straightforwardly extrapolated from the temperature of the structural $O^*$ to $O'$ transition observed in the paramagnetic phase for $x=0.10-0.14$. The temperature of the metal-insulator transition in the ferromagnetic phase follows very closely the decreased-magnetization anomalies in the magnetization measurements. Thus, the low-temperature metal-insulator resistive transition can be identified with the vestiges of the structural $O^*$ to $O'$ transition in the ferromagnetic phase. For $x=0.165$ and 0.17 samples, additional increases of resistivity (denoted by inverted triangles) can be seen on cooling in the paramagnetic phase at 310 and 290 K, respectively. These increases of resistivity correspond to the structural transformation from the rhombohedral $R$ to the orthorhombic $O^*$ structure.[12,25,38] Since the structural $R$ to $O^*$ transition temperature decreases and the ferromagnetic transition temperature increases with increasing $x$, the transition lines cross around 280 K for compositions between $x=0.17$ and 0.175. The vestige of the structural $R$ to $O^*$ transition in the ferromagnetic phase can be observed as a weak resistive anomaly in the metallic phase at $\sim$200 K for $x=0.175$. Similar anomalies of resistivity were seen at 155 K for single crystals with $x=0.18$.[12]

The resistivity for samples with $x>0.175$ is metallic for all temperatures below the ferromagnetic transition. With increase of $x$, the Curie temperature continues to increase linearly to values above 300 K for $x=0.2$. The resistivity for the rhombohedral phase above the Curie temperature is only weakly increasing with decreasing temperature and becomes almost temperature independent for $x=0.2$, consistent with the observation of a paramagnetic and metallic phase at high temperatures for $x>0.26$.[12]

## STRUCTURAL PROPERTIES

To relate physical properties to more precise structural information, neutron powder diffraction was done as a function of temperature for samples with $x=0.11$, 0.135, 0.165, and 0.185. The neutron diffraction technique can provide valuable data about the positions and coherent displacements of oxygen atoms. This data can be used to accurately determine bond lengths and bond angles. In addition, this technique can supply information regarding incoherent, static or dynamic, oxygen displacements from examination of anisotropic Debye-Waller parameters. The pattern of the coherent displacements and the symmetry of the incoherent displacements can be used to obtain information about polaronic electron-phonon interactions in both the paramagnetic and ferromagnetic phases.

Powder neutron-diffraction data were collected for the dense samples from 12 to 340 K using all detector banks at the SEPD, but only the higher resolution backscattering data ($\Delta d/d=0.035$) were analyzed. Rietveld structural refinements were carried out using the GSAS code[39] over the $d$-spacing range $0.5<d<4.0$ Å. The background was modeled using an eight-term cosine Fourier series. The diffraction peaks were described using a two-sided exponential that was convoluted with a Gaussian and a Lorenztian to describe the instrumental and sample contributions to the peak profile, respectively. For each pattern, atom positions and thermal parameters were refined. Based on previous reports for Sr-
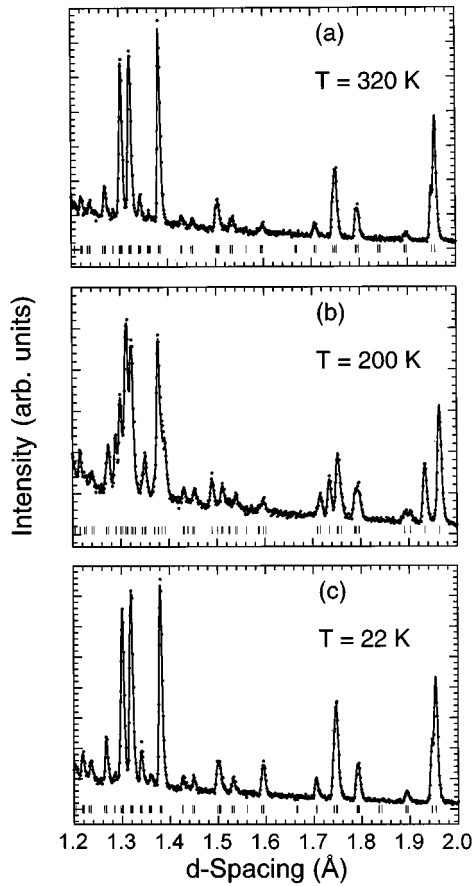
FIG. 7. Observed neutron powder-diffraction data and Rietveld calculated pattern for the $La_{0.89}Sr_{0.11}MnO_3$ sample at 320 K ($O*$, a), 200 K ($O'$, b), and 22 K ($O*$, c). Tick lines below the patterns indicate positions of allowed Bragg and magnetic reflections.

substituted materials, the patterns were indexed using an orthorhombic cell, space group *Pbnm*.[7–9,12] The observed and calculated patterns for the data taken at 320, 200, and 22 K for the $x = 0.11$ sample are shown in Fig. 7. Since the samples are ferromagnetic at 22 K the determined magnetic structure, space group $Pb'nm'$, is included in the calculated pattern shown in Fig. 7. The refined structural parameters are given in Table I for $x = 0.11$, 0.135, 0.165, and 0.185 samples at 12–22 K.

We will discuss the structural behavior of the $La_{1-x}Sr_xMnO_3$ samples in terms of the coherent (lattice parameters, bond lengths, and bond angles) and incoherent (anisotropic Debye-Waller) parameters. Figure 8 shows the temperature dependence of these parameters in the orthorhombic space group *Pbnm* for $x = 0.11$. The $b$ and $c$ lattice parameters [see Fig. 8(a)] on cooling display an abrupt increase and decrease, respectively, at $T_S \sim 300$ K that correlates exactly with the temperature of the resistive anomaly and with the $O'$ to $O*$ structural transition seen in the x-ray diffraction as a function of increasing composition. The $a$ lattice parameter does not show a visible discontinuity. Within the *Pbnm* space group, there are two nonequivalent oxygen positions, apical and equatorial, which characterize distortion of the $Mn-O_6$ octahedron in terms of lengths of the Mn-O bonds. Figure 8(b) shows the three Mn-O bond lengths and their average. The equatorial bonds show an abrupt change

that confirms development of a large coherent JT distortion on cooling; i.e., the transition from the $O*$ phase to the $O'$.[13] The apical Mn-O bond shows a somewhat smaller decrease. At the transition from the $O*$ to the $O'$ phase, the coherent JT distortion rapidly increases from $\sim 0.05$ Å to $\sim 0.13$ Å. The changes of lattice parameters and bond lengths are in agreement with neutron-diffraction data for a single crystal of $La_{0.875}Sr_{0.125}MnO_3$.[24] The average bond length shows a slight increase consistent with more insulating bonds in the $O'$ phase. Bond angles, shown in Fig. 8(c), display a slight decrease, i.e., a departure from a straight 180° bond is increased for the $O'$ phase, which also agrees with a weaker orbital overlap of the Mn-O bonds.

The temperature dependences of the components of the anisotropic Debye-Waller factor for the apical oxygen are shown in Fig. 8(d). The incoherent JT distortions that can be derived from the Debye-Waller factors are large and some of them show substantial reductions at the $O*$ to $O'$ transition. The incoherent distortion in the direction of the Mn-O bond ($U_{par}$) shows a sharp drop below 300 K. Incoherent distortions in the plane perpendicular to the Mn-O bond ($U_{perp}$) are larger but show almost linear temperature dependence. Similar behavior of the incoherent distortions parallel and perpendicular to the Mn-O bond was observed for the equatorial oxygen. The temperature dependences of these incoherent distortions in directions parallel and perpendicular to the Mn-O bond imply the presence of large local JT distortions for the $Mn-O_6$ octahedron in the $O*$ phase. The magnitude of the distortions, $\sim \sqrt{U}(O_{eq})_{perp} \sim 0.1$ Å, suggests random, statically or dynamically, fully distorted octahedra. In the $O'$ phase, the random distortions decrease to $\sqrt{U}(O_{eq})_{perp} \sim 0.04$ Å at 150 K while the coherent JT distortions increase to $\sim 0.13$ Å. Thus, the $O*$ to $O'$ transition can be characterized as an order-disorder transition. The randomly disordered highly distorted $Mn-O_6$ octahedrons in the $O*$ phase undergo long-range ordering in the $O'$ phase. It appears that the size and concentration of the JT-distorted $Mn-O_6$ octahedra do not change significantly during the transition. Consequently, a moderate increase of the resistivity in the $O'$ phase results from the long-range JT-polaron ordering, and possibly, a slight band narrowing due to an increased Mn-O bond length and decreased Mn-O-Mn bond angle.

On further cooling, at temperatures below $T_s \approx 150$ K, a seemingly "reverse" structural transition is observed from the $O'$ phase to a phase resembling the high-temperature ($T > 300$ K) orthorhombic $O*$ structure. A coexistence of both the $O'$ and $O*$ phases was observed as two sets of distinct lines over the small range of temperatures 120–140 K (Fig. 8). At this transition, the $b$ and $c$ lattice parameters abruptly decrease and increase, respectively, and the $a$ lattice parameter shows a weak discontinuity. These changes of the lattice parameters are in agreement with the neutron-diffraction data for a crystal of $La_{0.875}Sr_{0.125}MnO_3$, which displays similar behavior.[24] The equatorial Mn-O bonds display an abrupt decrease of the coherent JT distortion. The apical Mn-O bond shows a somewhat smaller decrease. The resulting coherent JT distortion thus decreases to $\sim 0.065$ Å, which is somewhat larger than the distortion in the paramagnetic state for the $O*$ structure, $\sim 0.05$ Å. The unequal bond lengths observed for our $x = 0.11$ sample below 120 K are in

TABLE I. Refined structural parameters from neutron powder diffraction for orthorhombic, *Pbnm*, $La_{1-x}Sr_xMnO_3$, $x=0.11$ at 22 K, $x=0.13$ at 15 K, $x=0.165$ at 12 K, and $x=0.185$ at 15 K.

| | | $x=0.11$ | $x=0.13$ | $x=0.165$ | $x=0.185$ |
|---|---|---|---|---|---|
| $a$ | (Å) | 5.5312(2) | 5.5308(1) | 5.5291(1) | 5.52934(6) |
| $b$ | (Å) | 5.5241(2) | 5.5137(1) | 5.4937(1) | 5.48160(7) |
| $c$ | (Å) | 7.7844(2) | 7.7837(2) | 7.7716(1) | 7.7593(1) |
| $V$ | (Å$^3$) | 237.85(1) | 237.37(7) | 236.06(1) | 235.180(6) |
| $\mu$ | ($\mu_B$) | 3.42(3) | 3.46(4) | 3.5(1) | 3.56(5) |
| Mn | $u_{iso}$(Å$^2$) | 0.0003(3) | 0.0007(2) | 0.0004(2) | 0.0002(2) |
| La/Sr | $x$ | 0.0048(4) | 0.0052(3) | 0.0041(3) | 0.0034(2) |
| | $y$ | 0.4754(2) | 0.4778(2) | 0.4825(2) | 0.4869(2) |
| | $u_{iso}$(Å$^2$) | 0.0010(2) | 0.0009(2) | 0.0008(1) | 0.0007(1) |
| O($a$) | $x$ | 0.0679(4) | 0.0657(4) | 0.0630(3) | 0.0609(2) |
| | $y$ | −0.0084(4) | −0.0083(4) | −0.0062(4) | −0.0056(3) |
| | $u_{11}$(Å$^2$) | 0.0032(8) | 0.0041(7) | 0.0034(5) | 0.0015(3) |
| | $u_{22}$(Å$^2$) | 0.005(1) | 0.004(1) | 0.0035(9) | 0.0046(7) |
| | $u_{33}$(Å$^2$) | 0.0056(9) | 0.0056(9) | 0.0037(8) | 0.0034(6) |
| | $u_{12}$(Å$^2$) | 0.0006(7) | −0.0003(7) | 0.0009(6) | −0.0009(5) |
| O($e$) | $x$ | 0.2710(4) | 0.2698(3) | 0.2667(2) | 0.2638(2) |
| | $y$ | 0.2205(3) | 0.2230(3) | 0.2297(2) | 0.2351(2) |
| | $z$ | −0.0350(2) | −0.0348(2) | −0.0336(2) | −0.0324(1) |
| | $u_{11}$(Å$^2$) | 0.0057(8) | 0.0057(7) | 0.0032(5) | 0.0014(3) |
| | $u_{22}$(Å$^2$) | 0.0032(6) | 0.0026(5) | 0.0036(5) | 0.0028(4) |
| | $u_{33}$(Å$^2$) | 0.0043(5) | 0.0050(5) | 0.0055(4) | 0.0059(3) |
| | $u_{12}$(Å$^2$) | 0.0001(4) | 0.0003(5) | 0.0004(4) | −0.0007(3) |
| | $u_{13}$(Å$^2$) | −0.0001(5) | −0.0002(5) | 0.0001(5) | 0.0002(4) |
| | $u_{23}$(Å$^2$) | 0.0000(5) | 0.0000(5) | 0.0010(5) | 0.0013(4) |
| $R_{WP}$ | (%) | 7.72% | 8.76% | 6.71% | 6.1% |
| $\chi^2$ | (%) | 3.07 | 2.93 | 3.14 | 2.24 |

disagreement with the $x=0.125$ single-crystal data that showed bonds of equal magnitude.[24] The average Mn-O bond length displays a small decrease consistent with less insulating bonds in the $O^*$ phase. Also the bond angles display small increases in agreement with a stronger orbital overlap of the Mn-O bonds for the $O^*$ phase. Both effects would lead to a small band widening.

The temperature dependences of the anisotropic Debye-Waller parameters show that incoherent JT distortions again become large below 150 K. The magnitude of the distortions, ~0.08 Å, confirms the presence of fully distorted octahedrons. Thus, the reverse transition can be characterized again as an order-disorder transition; i.e., the long-range ordered and highly distorted Mn-$O_6$ octahedra in the $O'$ phase disorder below 150 K in the $O^*$ phase. The size and concentration of the JT-distorted Mn-$O_6$ octahedrons do not change significantly during the reverse transition; only the long-range order is suppressed.

The reverse $O'$ to $O^*$ structural transition emerges within the lower temperature range of the magnetoresistive transition where a ferromagnetic state is almost fully established. It seems that development of the ferromagnetic state gradually suppresses the coherent JT distortion in the $O'$ phase. The magnitude of the resistive anomaly at the reverse transition, 130–170 K, is substantially more pronounced than the anomaly at 300 K. The resistive anomaly at 300 K is a result of a purely structural transition while the anomaly at 130–170 K is a result of both structural and ferromagnetic transi-

tions. Consequently, a less resistive state below 130 K results from both removal of the spin scattering by the double-exchange mechanism and suppression of the coherent JT-polaron ordering in the $O^*$ phase. The magnitudes of changes of the average bond length and bond angle indicate a larger increase of the bandwidth during a magnetoresistive-structural transition at 130–170 K than the bandwidth decrease during the structural-resistive transition at 300 K.

Similar temperature-dependent neutron-diffraction measurements performed for the $x=0.13$ composition confirmed the correlation between structural and physical properties that was observed for the $x=0.11$ sample. According to the resistive and magnetic measurements, the $x=0.13$ composition should display the $O^*$ to $O'$ transition on cooling around 265 K, and a reverse $O'$ to $O^*$ transition below 195 K. Figures 9(a)–9(d) show the lattice parameters, bond lengths, bond angles, and anisotropic Debye-Waller parameters for $x=0.13$. All coherent and incoherent parameters show the anticipated behavior. Structural changes are less dramatic than for the $x=0.11$ sample. For example, the coherent JT distortion increases from ~0.04 Å to ~0.11 Å during the $O^*$ to $O'$ transition and decreases back to ~0.06 Å at the reverse $O'$ to $O^*$ transition. The less dramatic changes are in agreement with a smaller range of temperatures where the $O'$ phase persists, and with the known decrease of the coherent JT distortion for increased $x$.[12,27] The observed relationships corroborate the conclusion that the $O^*$ to $O'$ transition is an order-disorder transition during
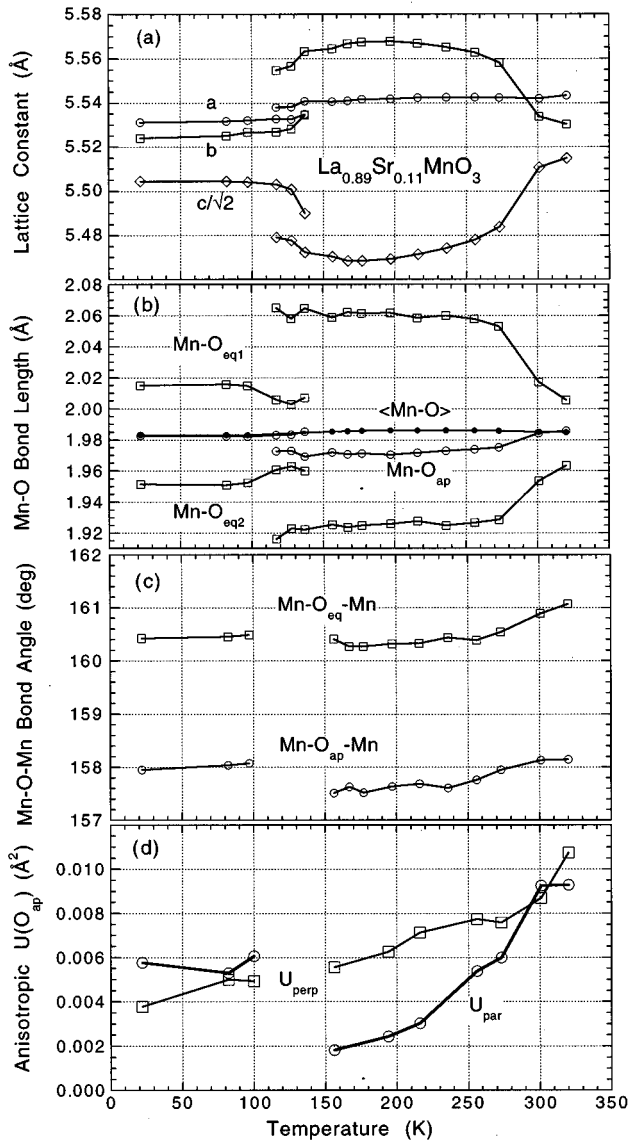
FIG. 8. Refined coherent and incoherent structural parameters from neutron powder-diffraction measurements as a function of temperature for $La_{0.89}Sr_{0.11}MnO_3$: (a) Lattice parameters, (b) Mn-O bond lengths and their average value, (c) Mn-O-Mn bond angles, (d) Anisotropic Debye-Waller factors.

which randomly disordered and highly distorted Mn-O$_6$ octahedrons in the $O^*$ phase undergo a long-range ordering in the $O'$ phase. During the reverse $O'$ to $O^*$ transition, which follows the ferromagnetic transition, the long-range ordering of highly distorted Mn-O$_6$ octahedra is suppressed. The resistive properties confirm that the coherent ordering of distorted Mn-O$_6$ octahedra increases resistivity via long-range polaron localization and the ferromagnetic transition lowers the resistivity by removal of the spin scattering according to the double-exchange mechanism. The structural response below $T_C$ to the ferromagnetic transition appears to be universal for the $La_{1-x}Sr_xMnO_3$ system in the orthorhombic $O'$ structure.

For both compositions, $x=0.11$ and 0.13, the $O^*$ to $O'$ transition on cooling is present in the paramagnetic phase while the ferromagnetic transition develops in the $O'$ structure. To observe the structural response to the ferromagnetic
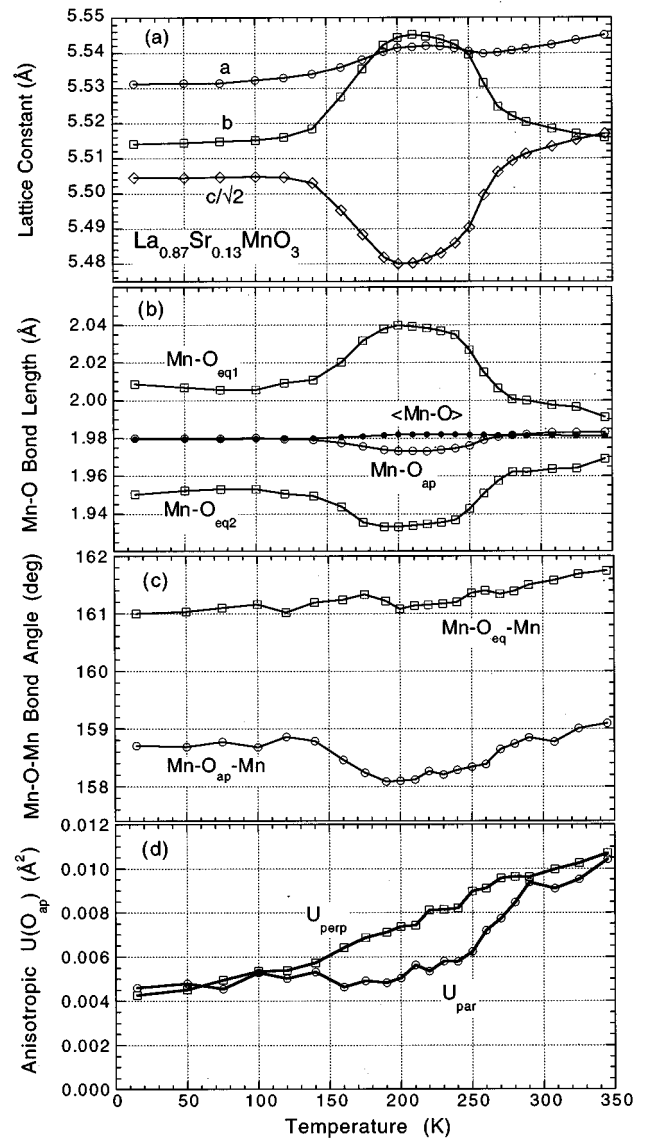
FIG. 9. Same as Fig. 8 for $La_{0.87}Sr_{0.13}MnO_3$.

transition in the $O^*$ structure and to detect vestiges of the structural $O^*$ to $O'$ transition in the ferromagnetic phase, temperature-dependent neutron-diffraction measurements were performed for the $x=0.165$ sample. Figures 10(a)–10(d) show the relevant coherent and incoherent parameters. The sample is rhombohedral at high temperature, 340 K. Since there is only one oxygen atom position for the rhombohedral symmetry, there is one Mn-O-Mn bond angle, and all Mn-O bonds are of equal length; i.e., there is (by symmetry) no coherent JT distortion for this phase. The measured Debye-Waller parameter is isotropic and similar in magnitude to that previously observed for the $O^*$ phase, indicating the presence of incoherently distorted Mn-O$_6$ octahedra in the rhombohedral phase.[20] On cooling below 340 K, the rhombohedral structure changes to orthorhombic $O^*$ with a small coherent JT distortion, $\sim 0.01$ Å. The average bond length increases significantly and the average bond angle decreases rapidly. These structural changes are consistent with increased resistivity upon the transition from the rhombohedral to $O^*$ phase seen for our samples and for single crystals at similar compositions and temperatures.[12,25,38]
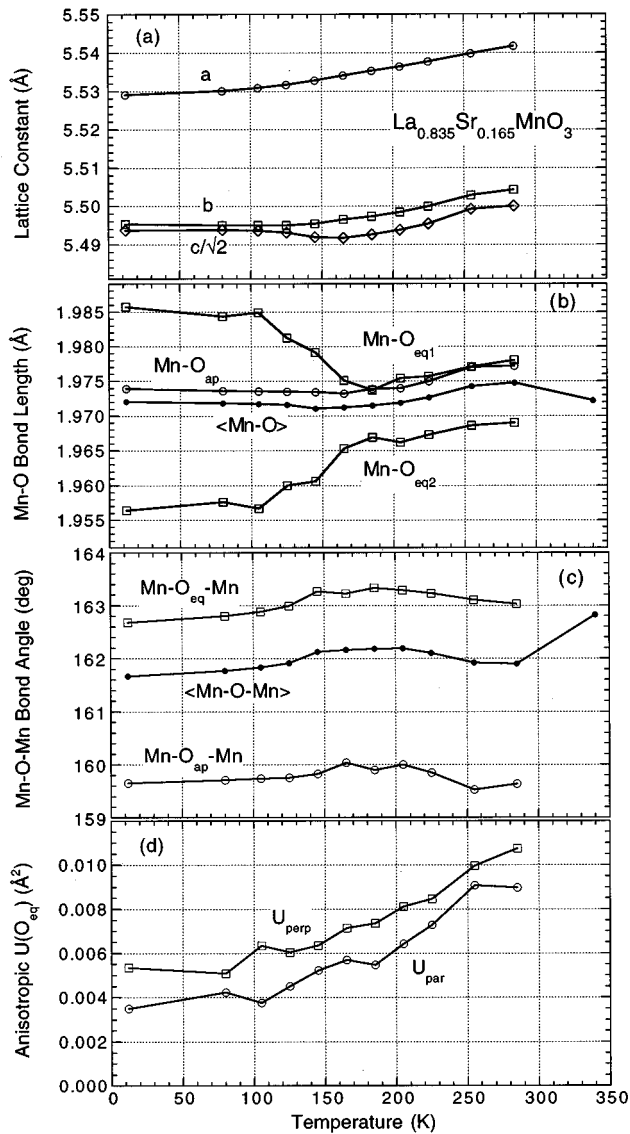
FIG. 10. Same as Fig. 8 for $La_{0.835}Sr_{0.165}MnO_3$.

On further cooling an abrupt decrease of the lattice parameters appears at the ferromagnetic transition temperature $T_C \sim 256$ K. The individual Mn-O bond lengths do not show clear drops below $T_C$ and the coherent Jahn-Teller distortion remains practically unchanged. However, below $T_C$, the average Mn-O bond length shows a slight decrease, $\sim 0.003$ Å. Simultaneously, the average bond angle displays a slight increase, $\sim 0.4$ degrees. The decrease of the average bond lengths and the increase of the average bond angle below $T_C$ are consistent with the creation of itinerant electrons and the development of metallic bonds in the ferromagnetic phase. The incoherent JT distortion along the Mn-O bond shows a slight decrease. These changes, although smaller, are similar to those seen at the ferromagnetic transition for the $La_{1-x}Ca_xMnO_3$ system with the same $O^*$ structure but for different compositions and temperatures, $x=0.22$ ($T_C \sim 186$ K) and 0.25 ($T_C \sim 240$ K).[40,41] The sharp drops of resistivity at the ferromagnetic transition can be explained, thus, as resulting from removal of charge localization below $T_C$ by a strong electron-phonon JT coupling and a narrowing

of the bandwidth in addition to removal of the spin scattering by double exchange. The structural response at $T_C$ to the ferromagnetic transition appears to be universal for the $O^*$-structure-type for both Sr- and Ca-substituted materials.

On cooling below $\sim 160$K, an additional structural change takes place in the ferromagnetic phase. The temperature range of this structural change correlates very well with the resistive and magnetic anomalies which can be clearly identified with the vestiges of the structural $O^*$ to $O'$ change. During the transition, the $c$ lattice parameter abruptly increases. The $b$ lattice parameter shows a smaller increase while the $a$ lattice parameter does not show a visible discontinuity. The equatorial bonds show an abrupt change that indicates development of a coherent JT distortion. The apical Mn-O bond shows a smaller anomaly. The resulting coherent JT distortion increases only slightly from $\sim 0.01$–$\sim 0.03$ Å. All these changes are consistent with the $O^*$ to $O'$ transition that is suppressed in the ferromagnetic state, i.e., in the ferromagnetic state the orthorhombic structure is more alike the paramagnetic $O^*$ phase than the $O'$ phase. The relatively small value of the coherent JT distortion at 10 K indicates a decrease of the coherent distortion with increased $x$ for the $O^*$ phase in the ferromagnetic state similar to the decrease of the larger coherent JT distortions for the $O'$ phase in the paramagnetic state. The Debye-Waller parameter parallel to the Mn-O bond at 10 K is slightly smaller in value, $\sim 0.004$ Å, than that observed for $x=0.11$ and 0.13 samples, $\sim 0.005$ and 0.006 Å, respectively, indicating small decrease of the large incoherent JT distortions for the $O^*$ phase in the ferromagnetic state with increasing $x$. The average bond length shows a slight increase and the average bond angle displays a slight decrease on cooling. These changes are, again, consistent with the more insulating bonds in the $O'$ phase as seen by the metal-insulator resistive transition.

The structural response to the ferromagnetic transition in the rhombohedral structure and vestiges of the structural $R$ to $O^*$ transition in the ferromagnetic phase were measured for the $x=0.185$ sample. Figures 11(a)–11(d) show the relevant coherent and incoherent parameters. At the ferromagnetic transition at 290 K, small decreases appear for the rhombohedral lattice parameter and the Mn-O bond length. The bond angle displays a slight increase, $\sim 0.2$ degrees. Again, these changes are consistent with the creation of the itinerant electrons and the development of metallic bonds in the ferromagnetic phase. The incoherent distortions both along and perpendicular to the Mn-O bond are quite large above $T_C$ and show a slight decrease suggesting the presence of smaller incoherent JT distortions for the metallic and ferromagnetic phase.

On cooling below 150 K, the $R$ structure transforms to $O^*$ with a slightly increased average Mn-O bond length and decreased average Mn-O-Mn bond angle. During the transition a very small coherent JT distortion develops and the incoherent JT distortion decreases further. At the lowest temperatures studied, the incoherent distortion along the Mn-O bond reaches a value about half that observed for $x=0.11$, 0.13, and 0.165 at the same temperature. Hence, we assign the $x=0.185$ composition to an ''incoherent-small'' regime at this temperature in Fig. 1. The changes of coherent and incoherent JT distortions at $R/O^*$ transition are small
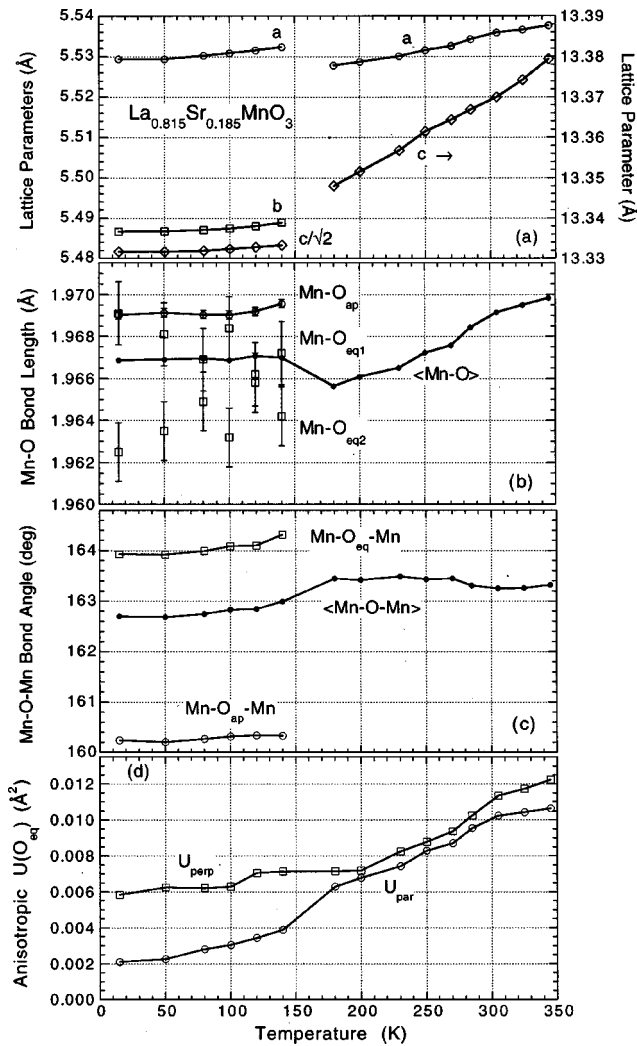
FIG. 11. Same as Fig. 8 for $La_{0.815}Sr_{0.185}MnO_3$.

enough and partially compensating such that the $x = 0.185$ composition remains metallic in the $O^*$ phase.

Based on physical properties and structural data, the following structure-properties relationships were developed for moderately substituted $La_{1-x}Sr_xMnO_3$. As shown in Fig. 1, in the high-temperature paramagnetic regime, three structural phases are present: orthorhombic *Pbnm* structure ($O'$), characterized by the large coherent orbital ordering of the JT type and small incoherent JT distortions; orthorhombic *Pbnm* structure ($O^*$) characterized by a small coherent JT-orbital ordering and large incoherent JT distortions; rhombohedral $R\bar{3}m$ structure ($R$) characterized by the absence of a coherent JT-orbital ordering and large incoherent JT distortions. For $0.10 < x < 0.145$, during the ferromagnetic transition, the orthorhombic $O'$ phase changes to an orthorhombic $O^*$ phase characterized by suppressed coherent JT-orbital ordering and large incoherent JT distortions. For $0.15 < x < 0.17$, on cooling during the ferromagnetic transition the insulating orthorhombic $O^*$ phase changes to a metallic $O^*$ phase

characterized by small coherent and small incoherent JT distortions. Below the Curie temperature, in the ferromagnetic phase, this orthorhombic $O^*$ phase changes to an orthorhombic $O^*$ phase characterized by suppressed coherent JT-orbital ordering and large incoherent JT distortions. For $0.175 < x < 0.20$, on cooling during the ferromagnetic transition the semiconducting $R$ phase changes to a metallic $R$ phase with small incoherent JT distortions. Below the Curie temperature, in the ferromagnetic phase, this $R$ structure changes to an orthorhombic *Pbnm* structure $O^*$ characterized by small coherent JT-orbital ordering and small incoherent JT distortions that is still metallic. Development of ferromagnetic order, thus, suppresses the coherent JT distortions for the $O'$ phase and incoherent distortions for the $O^*$ and $R$ phases.

## CONCLUSION

The data clearly show that the ferromagnetic phase has lower resistivity than the paramagnetic phase. However, the ferromagnetic transition is accompanied by structural changes that can also cause a decrease of resistivity. The suppression of coherent JT distortions lowers the resistivity but is not sufficient to produce a metallic phase unless large incoherent JT distortions are also removed. Over a limited range of compositions around $x \approx 0.125 = 1/8$, a high resistance phase with decreased ferromagnetic moment is present. This phase may be a charge-ordered phase for which a breathing-mode electron-phonon interaction dominates and leads to charge localization. It is interesting to observe that the ferromagnetic $T_C$ appears to be slightly depressed from a linear increase with $x$ near $x \approx 0.125$ suggesting the suppression of ferromagnetism by breathing-mode fluctuations. For other compositions, the electron-phonon Jahn-Teller interactions and the magnetic superexchange and double-exchange interactions are of similar strength. These interactions compete for the same $e_g$ electrons and, thus, lead to colossal spin-charge-lattice coupling.

For $0.1 < x < 0.2$, a competition between the electron-phonon Jahn-Teller and breathing-mode interactions, and the magnetic superexchange and double-exchange interactions results in a rich structure-property phase diagram. The structural, magnetic, and resistive data show that the development of ferromagnetic order competes with coherent JT distortions for the $O'$ phase and with incoherent distortions for the $O^*$ phase. The data confirm that charge localization above $T_C$ arises from the spin scattering, a strong electron-phonon coupling mediated by the Jahn-Teller splitting of the $e_g$ states, and possibly a narrowing of the bandwidth. The structural response at $T_C$ to the ferromagnetic transition is universal for the $O^*$ structure type since it is the same as for the Ca-substituted materials.

[1] R. M. Kusters, J. Singelton, D. A. Keen, R. McGreevy, and W. Hayes, Physica B **155**, 362 (1989).

[2] C. Zener, Phys. Rev. **82**, 403 (1951).

[3] P. W. Anderson and H. Hasegawa, Phys. Rev. **100**, 675 (1955).

[4] J. B. Goodenough, *Magnetism and Chemical Bond* (Wiley, New York, 1963).

[5] P. A. Cox, *Transition Metal Oxides* (Clarendon, Oxford, 1995).

[6] E. O. Wollan and W. C. Koehler, Phys. Rev. **100**, 545 (1955).

[7] J. B. A. A. Elemans, B. Van. Laar, K. R. Van Der Veen, and B. O. Loopstra, J. Solid State Chem. **3**, 238 (1971).

[8] Q. Huang, A. Santoro, J. W. Lynn, R. W. Erwin, J. A. Borchers, J. L. Peng, and R. L. Greene, Phys. Rev. B **55**, 14 987 (1997).

[9] J. Rodriguez-Carvajal, M. Hennion, F. Moussa, A. H. Moudden, L. Pinsard, and A. Revcolevschi, Phys. Rev. B **57**, R3189 (1998).

[10] Y. Murakami, J. P. Hill, D. Gibbs, M. Blume, I. Koyama, M. Tanaka, H. Kawata, T. Arima, Y. Tokura, K. Hirota, and Y. Endoh, Phys. Rev. Lett. **81**, 582 (1998).

[11] G. H. Jonker and J. H. Van Santen, Physica (Amsterdam) **16**, 337 (1950).

[12] A. Urushibara, Y. Moritomo, T. Arima, A. Asamitsu, G. Kido, and Y. Tokura, Phys. Rev. B **51**, 14 103 (1995).

[13] H. Kawano, R. Kajimoto, and H. Yoshizawa, Phys. Rev. B **53**, R14 709 (1996).

[14] J.-S. Zhou, J. B. Goodenough, A. Asamitsu, and Y. Tokura, Phys. Rev. Lett. **79**, 3234 (1997).

[15] Y. Moritomo, A. Asamitsu, and Y. Tokura, Phys. Rev. B **56**, 12 190 (1997).

[16] A. J. Millis, P. B. Littlewood, and B. I. Shraiman, Phys. Rev. Lett. **74**, 5144 (1995).

[17] A. J. Millis, B. I. Shraiman, and R. Mueller, Phys. Rev. Lett. **77**, 175 (1996).

[18] H. Roder, J. Zhang, and A. R. Bishop, Phys. Rev. Lett. **76**, 1356 (1996).

[19] J. F. Mitchell, D. N. Argyriou, C. D. Potter, D. G. Hinks, J. D. Jorgensen, and S. D. Bader, Phys. Rev. B **54**, 6172 (1996).

[20] D. Louca, T. Egami, E. L. Brosha, H. Roder, and A. R. Bishop, Phys. Rev. B **56**, R8475 (1997).

[21] J. A. M. Van Roosmalen, P. van Vlaanderen, E. H. P. Cordfunke, W. L. Ijdo, and D. J. W. Ijdo, J. Solid State Chem. **114**, 516 (1995).

[22] P. G. Radaelli, M. Marezio, H. Y. Hwang, S.-W. Cheong, and B. Batlogg, Phys. Rev. B **54**, 8992 (1996).

[23] A. Asamitsu, Y. Moritomo, Y. Tomioka, T. Arima, and Y. Tokura, Nature (London) **373**, 407 (1995).

[24] L. Pinsard, J. Rodriguez-Carvajal, A. H. Moudden, A. Anane, A. Revcolevschi, and C. Dupas, Physica B **234-236**, 856 (1997).

[25] Y. Yamada, O. Hino, S. Nohdo, R. Kanao, T. Inami, and S. Katano, Phys. Rev. Lett. **77**, 904 (1996).

[26] J. A. M. Van Roosmalen and E. H. P. Cordfunke, J. Solid State Chem. **110**, 106 (1994).

[27] B. Dabrowski, K. Rogacki, X. Xiong, P. W. Klamut, R. Dybzinski, J. Shaffer, and J. D. Jorgensen, Phys. Rev. B **58**, 2716 (1998).

[28] J. A. M. Van Roosmalen, E. H. P. Cordfunke, R. B. Helmholdt, and H. W. Zandbergen, J. Solid State Chem. **110**, 100 (1994).

[29] J. A. M. Van Roosmalen and E. H. P. Cordfunke, J. Solid State Chem. **110**, 109 (1994).

[30] J. A. M. Van Roosmalen and E. H. P. Cordfunke, J. Solid State Chem. **110**, 113 (1994).

[31] J. Toepfer and J. B. Goodenough, Chem. Mater. **9**, 1467 (1997).

[32] P. Schiffer, A. P. Ramirez, W. Bao, and S.-W. Cheong, Phys. Rev. Lett. **75**, 3336 (1995).

[33] M. Hervieu, R. Mahesh, N. Rangavittal, and C. N. R. Rao, Eur. J. Solid State Inorg. Chem. **32**, 79 (1995).

[34] B. Dabrowski, R. Dybzinski, Z. Bukowski, O. Chmaissem, and J. D. Jorgensen (unpublished).

[35] J. D. Jorgensen, J. Faber, Jr., J. M. Carpenter, R. K. Crawford, J. R. Haumann, R. L. Hitterman, R. Kleb, G. E. Ostrowski, F. J. Rotella, and T. G. Worlton, J. Appl. Crystallogr. **22**, 321 (1989).

[36] X. Xiong, Z. Bukowski, S. Kolesnik, B. Dabrowski, R. Dybzinski, O. Chmaissem, C. W. Kimball, and J. D. Jorgensen (unpublished).

[37] K. Ghosh, R. L. Greene, S. E. Lofland, S. M. Bhagat, S. G. Karabashev, D. A. Shulyatev, A. A. Arsenov, and Y. Mukovskii, Phys. Rev. B **58**, 8206 (1998).

[38] A. J. Campbell, G. Balakrishnan, M. R. Lees, D. McK. Paul, and G. J. McIntyre, Phys. Rev. B **55**, R8622 (1997).

[39] A. C. Larson and R. B. von Dreele, General Structure Analysis System, University of California, 1985–1990.

[40] B. Dabrowski, Z. Bukowski, X. Xiong, K. Rogacki, P. W. Klamut, R. Dybzinski, J. E. Siewenie, C. W. Kimball, and J. D. Jorgensen (unpublished).

[41] P. G. Radaelli, G. Iannone, M. Marezio, H. Y. Hwang, S.-W. Cheong, J. D. Jorgensen, and D. N. Argyriou, Phys. Rev. B **56**, 8265 (1997).